AIMS Materials Science, 11(6): 1096–1124.
DOI: 10.3934/matersci.2024053
Received: 17 July 2024
Revised: 05 November 2024
Accepted: 13 November 2024
Published: 28 November 2024

http://www.aimspress.com/journal/Materials

Research article

Banksia Ashbyi-engineered facile green synthesis of magnetite nanoparticles: Characterization, and determination of micro-strain, stress, and physical parameters by X-ray-based Williamson-Hall analysis

Gérrard Eddy Jai Poinern[1,*], A F M Fahad Halim[1], Derek Fawcett[1], Peter Chapman[2] and Rupam Sharma[3]

[1] School of Engineering and Energy, Murdoch University, Western Australia 6150, Australia
[2] Department of Chemistry, Curtin University, Perth, Western Australia
[3] ICFE-Central Institute of Fisheries Education, Mumbai, India

* **Correspondance:** Email: g.poinern@murdoch.edu.au.

Abstract: Magnetite nanoparticles (MNPs) were synthesized by a straightforward one-step biogenic process using a leaf extract taken from the Australian indigenous plant *Banksia ashbyi* (BA). Several advanced characterization techniques, such as X-ray diffraction (XRD), Fourier transform infrared spectroscopy (FT-IR), energy-dispersive spectroscopy (EDS), thermogravimetric analysis (TGA), and Raman spectroscopy were used to investigate the physical and chemical properties of synthesized MNPs. In addition, the size and morphology of the synthesized particles were examined using both focused ion beam scanning electron microscopy (FIBSEM) and transmission electron microscopy (TEM) methods. FT-IR analysis revealed the presence of a Fe–O band located at 551 cm^{-1}, which confirmed the formation of BA-MNPs. Both FIBSEM and TEM image analysis confirmed the nanoparticles were spherical in shape and had a mean diameter of 18 nm with a particle distribution that ranged between 13 and 23 nm. The strong iron (Fe) and oxygen (O) peaks seen in the EDS analysis also confirmed the formation of the MNPs. TGA analysis revealed the leaf extract not only acted as the reducing agent but also served as a capping agent. The XRD analysis revealed that the synthesized MNPs exhibited a high degree of crystallinity and did not contain any impurities. Furthermore, X-ray peak profile analysis using Williamson-Hall methods found the average crystallite size was 9.13 nm, with the crystal lattice experiencing a compressive stress of 546.5 MPa and an average micro-strain of 2.54×10^{-3}. In addition, other material properties such as density (5.260 kg/m^3), average Young's

modulus of elasticity (217 GPa), modulus of rigidity (90 GPa), and Poisson's ratio (0.235) were also estimated from the XRD data.

Keywords: magnetite nanoparticles; green biosynthesis; Williamson-Hall analysis; material properties; micro-strain; compressive stress

1. Introduction

In recent years, ferroic materials have attracted considerable scientific interest due to their intriguing and unique physical and chemical properties. In particular, magnetite (Fe_3O_4) exhibits distinctive structural, electronic, and magnetic properties [1]. Bulk scale magnetite displays a cubic-inverse spinel arrangement, while magnetite nanoparticles (MNPs) have a mixed spinel form due to increased surface strains. The mixed spinel form also results in two distinct crystallographic sites, namely tetrahedral and octahedral. The distribution of divalent (Fe^{2+}) and trivalent (Fe^{3+}) cations in the respective tetrahedral and octahedral sites plays an important part in influencing the properties of ferrite materials [2]. In turn, these properties influence the type of function that MNPs can deliver in specific applications. To date, MNPs have been used in a wide variety of applications, including: (1) imaging agents in magnetic resonance (MRI) analysis [3–7]; (2) solid component in ferro-fluids [4]; (3) agents in hyperthermia therapy [3,4,7–9]; (4) carrier agents in bio-sensing and diagnosis [7,10,11]; (5) drug delivery platforms for pharmaceuticals [3,4,7,10–13]; (6) adjuvant and carrier agent in cancer treatments [7–9,14,15]; (7) electronics and data storage devices [15,16]; (8) catalyst supports [4,15,17,18]; (9) incorporated into magnetic paints and inks [15,19]; (10) components in energy storage systems [20–23]; and (11) adsorbents for the removal of contaminants from wastewater [18,24–27].

The wide variety of applications in which MNPs are utilized is a direct result of their size, composition, purity, and material properties. Importantly, nanoparticle size and its properties can be regulated by the type of fabrication process used in its manufacture. MNPs can be generated by either top-down or bottom-up methods. Top-down methods include several techniques, such as photolithography, ball milling, and grinding [28]. Bottom-up methods include pyrolysis [29], micro-emulsion [30], hydrothermal/solvo-thermal [1,31], sol-gel [32], sonochemical and microwave-assisted synthesis [33], chemical co-precipitation [34,35], and biosynthesis [29]. Furthermore, in recent years, there has been significant scientific interest in developing biological synthesis methods. These methods have the potential to replace several conventional chemical and physical methods and deliver better, greener, and less energy-intensive synthesis procedures [36]. Many of these conventional chemical and physical methods also have disadvantages like high manufacturing costs, the usage and disposal of harmful chemicals, and the creation of harmful by-products [37–39]. Thus, using alternative biogenic methods and the principle of green chemistry avoids these disadvantages. Biogenic synthesis has focused mainly on two types of biological entities, namely bacterial and plant-based techniques [39,40]. In recent years, a significant research effort has focused on plant-based techniques to produce nanoparticles. Studies have shown that extracts taken from stems, leaves, fruits, and seeds can be used to synthesize nanoparticles [40–43]. Nanoparticle synthesis via plant extracts is due to the presence of phytochemicals (e.g., amino acids, polyphenols, or reducing sugars), which act as stabilizing and reducing agents [43].

One bottom-up method for generating MNPs that has attracted significant interest in recent years involves iron salt hydroxylation in alkaline solutions followed by the dehydration of the resulting hydroxides. The method's advantages include: (1) use of readily available precursors; (2) being a straightforward chemical synthesis process; (3) not relying on complex and expensive laboratory equipment; (4) being more eco-friendly when compared to other methods that use hazardous chemicals and solvents, and (5) having the potential to be scaled up to facilitate large scale production [44].

The present exploratory study evaluates the use of a leaf extract taken from the Australian indigenous plant *Banksia ashbyi* (BA) as an agent for controlling nanoparticle size and size distribution when incorporated into the iron salt hydroxylation/dehydration method mentioned above. In this one-pot, facile, and green method, the aqueous BA leaf extract first assists in reducing the Fe precursors and then acts as a capping agent to form stable MNPs. Advanced characterization techniques were used to investigate the physiochemical and material properties of the MNPs. Fourier transform infrared spectroscopy (FT-IR), energy dispersive spectroscopy (EDS), and Raman spectroscopy confirmed the formation and chemical nature of the MNPs. UV-visible (UV-Vis) spectroscopy was used to determine the band gap, and thermo-gravimetric analysis (TGA) was used to evaluate the thermal stability of the MNPs. The geometric parameters of the MNPs including crystallite size and particle size were studied using X-ray diffraction (XRD), focused ion beam scanning electron microscopy (FIBSEM) and transmission electron microscopy (TEM). In addition, X-ray peak profile analysis using Williamson-Hall methods was used to determine strain, stress, and strain energy due to lattice deformation of the MNPs. XRD analysis was used to determine material properties, such as Young's modulus of elasticity, modulus of rigidity, and Poisson's ratio.

2. Theory: Estimating material properties from X-ray diffraction spectroscopy data

2.1. Crystallite size, lattice stress, and strain derived from Williamson-Hall analysis

Physical properties, such as crystallite size, lattice stress, lattice strain, and elastic modulus can be estimated from X-ray peak profile analysis using Williamson-Hall analysis. Peak broadening occurs in X-ray diffraction spectra due to instrumental effects and imperfect sample crystallinity. To correct for instrumental broadening and remove this aberration, it is necessary to collect a diffraction pattern using a standard material such as silicon. Then, the peaks in the silicon diffraction pattern are used to correct the corresponding peaks of the sample diffraction pattern using Eq 1 [45]:

$$\beta_{(hkl)} = \left[\beta^2_{(hkl)}\,(measured) - \beta^2_{(hkl)}\,(instrumental)\right]^{0.5} \tag{1}$$

Then, the crystalline size ($D_{(hkl)}$) of the sample is calculated using the Debye-Scherer formula presented in Eq 2 [46]:

$$D_{(hkl)} = \frac{k\lambda}{\beta_{(hkl)}\ \cos\theta_{(hkl)}} \tag{2}$$

In Eq 2, λ is the wavelength of the monochromatic X-ray beam, and k is the crystallite shape constant, which is 0.9 for spherical crystals with cubic unit cells. $\beta_{(hkl)}$ is the full width at half maximum (FWHM) of the peak at the maximum intensity, and $\theta_{(hkl)}$ is the peak diffraction angle that satisfies Bragg's law for the (h k l) plane. $D_{(hkl)}$ is the crystallite size of the sample. Eq 2 also shows that the crystalline

size ($D_{(hkl)}$) is dependent on the reciprocal of cosine θ. The crystallographic distance (d) between planes for given Miller indices h, k, and l can be estimated using Bragg's equation, as presented by Eq 3:

$$n\lambda = 2d \sin\theta \tag{3}$$

In Eq 3, n and θ represent the diffraction order (usually n = 1) and the Bragg angle, respectively. In the case of a cubic structure, the d spacing is related to the lattice constants and Miller indices h, k, and l through Eq 4. Thus, Eq 4 can be used to estimate the size of the respective lattice constants.

$$d = \frac{a}{\sqrt{h^2 + k^2 + l^2}} \tag{4}$$

Once the lattice constant (a) is determined, then the unit-cell volume can be estimated using Eq 5 [47]:

$$V = a^3 \tag{5}$$

Studies have shown that crystallite size and strain both contribute to the peak broadening and are independent of each other [45,46]. Both parameters can be expressed by Eq 6:

$$\beta_{(hkl)} = \beta_{(crystallite\ size)} + \beta_{(strain)} \tag{6}$$

The strain-induced peak broadening component of Eq 6 can be determined from Eq 7, which shows the strain (ε) is inversely proportional to tan (θ):

$$\varepsilon = \frac{\beta_{(hkl)}}{4 \tan\theta} \tag{7}$$

Thus, combining the crystallite size and strain-induced peak broadening components expressed in Eqs 2 and 7, Eq 8 below can be derived:

$$\beta_{(hkl)} = \frac{k\lambda}{D_{(hkl)} \cos\theta_{(hkl)}} + 4\varepsilon \tan\theta \tag{8}$$

Then, rearranging Eq 8 gives Eq 9. Both Eqs 8 and 9 form the basis of Williamson-Hall analysis of peak broadening effects seen in sample powders.

$$\beta_{(hkl)} \cos\theta = \frac{k\lambda}{D_{(hkl)}} + 4\varepsilon \sin\theta \tag{9}$$

Eq 9 represents the uniform deformation model (UDM), which assumes a uniform strain in all crystallographic directions and that material properties are independent of the direction along which measurements are made. When the resulting experimental measurements are plotted, with 4sinθ along the x-axis and $\beta(hkl)$ cosθ along the y-axis, the resulting graph gives a linear fit to the data. From the graph, strain (slope) and crystallite size (y-intercept) can be determined. The second Williamson-Hall analysis uses the uniform stress deformation model (USDM), which assumes the sample material follows Hooke's law. Thus, there is a linear relationship between the stress and strain, as seen in Hooke's law expressed by Eq 10.

$$E = \frac{\sigma}{\varepsilon} \tag{10}$$

In Eq 10, E is the elastic modulus, also known as Young's modulus of elasticity, and σ is the stress present in the crystallite structure. Incorporating Eq 10 into Eq 9 gives Eq 11, which is used in the (USDM) analysis.

$$\beta_{(hkl)} \cos\theta = \frac{k\lambda}{D_{(hkl)}} + \frac{4\sigma \sin\theta}{E_{(hkl)}} \tag{11}$$

In Eq 11, $E_{(hkl)}$ is the modulus of elasticity occurring perpendicular to the *(hkl)* crystal lattice plane. Because $E_{(hkl)}$ is dependent on the crystallographic direction, it must be calculated for each orientation within the cubic crystal structure, as seen in Eq 12 [48,49].

$$\frac{1}{E_{(hkl)}} = S_{11} - 2\left(S_{11} - S_{12} - \frac{1}{2}S_{44}\right)\left(l_1^2 l_2^2 + l_2^2 l_3^2 + l_3^2 l_1^2\right) \tag{12}$$

In Eq 12, S_{11}, S_{12}, and S_{44} are the elastic-compliances, and l_1, l_2, and l_3 are the orientation parameters derived from Eqs 13–15, respectively.

$$l_1 = h(h^2 + k^2 + l^2)^{-0.5} \tag{13}$$

$$l_2 = k(h^2 + k^2 + l^2)^{-0.5} \tag{14}$$

$$l_3 = l(h^2 + k^2 + l^2)^{-0.5} \tag{15}$$

In addition, the elastic compliances (S_{11}, S_{12}, and S_{44}) are related to the stiffness parameters (C_{11}, C_{12}, and C_{44}) of the material through Eqs 16–18 below.

$$S_{11} = \frac{(C_{11} + C_{12})}{(C_{11} - C_{12})(C_{11} + 2\,C_{12})} \tag{16}$$

$$S_{12} = \frac{-C_{12}}{(C_{11} - C_{12})(C_{11} + 2C_{12})} \tag{17}$$

$$S_{44} = \frac{1}{C_{44}} \tag{18}$$

Once the respective elastic-compliances and orientation parameters are derived, then the $E_{(hkl)}$ for each crystal plane can be calculated. Next, the respective $E_{(hkl)}$ values are then substituted into Eq 11. Then, by plotting $4\sin\theta/E_{(hkl)}$ along the x-axis and $\beta_{(hkl)} \cos\theta$ along the y-axis, the resulting graph gives a linear fit to the data. From the graph of the USDM data, the slope of the graph is the stress present in the sample and the y-intercept is the estimated crystallite size. However, in many cases, the assumption of homogeneity and isotropy in all crystallographic directions is not achieved. When strain energy density (u) is considered, the proportionality normally associated with the stress and strain relationship may no longer be independent. The strain energy density (u) can be calculated using Eq 19 presented below. When the strain energy density equation is rearranged and substituted into

Eq 9, the modified equation (using Eq 20) becomes the uniform deformation energy density model (UDEDM) [50].

$$u = \frac{\varepsilon^2 E_{(hkl)}}{2} \tag{19}$$

$$\beta_{(hkl)} \cos\theta = \frac{k\lambda}{D_{(hkl)}} + 4 \sin\theta \left(\frac{2u}{E_{(hkl)}}\right)^{\frac{1}{2}} \tag{20}$$

Thus, by plotting $4sin\theta(2/E_{(hkl)})^{1/2}$ along the x-axis and $\beta_{(hkl)}cos\theta$ along the y-axis, the resulting slope gives the lattice strain, and the y-intercept gives the crystallite size. Once the lattice strain is determined, the respective strain energy density value can be calculated.

2.2. Determining physical properties from XRD data

Further analysis of the XRD data can be used to determine physical properties such as: (1) density (ρ_{XRD}); (2) longitudinal (V_L), shear (V_S), and mean (V_m) wave velocities; (3) longitudinal modulus (L); (4) modulus of rigidity (G); (5) bulk modulus (B); and (6) Poisson's ratio of the sample material.

2.2.1. X-ray density (ρ_{XRD})

The X-ray density (ρ_{XRD}) is calculated using Eq 21, where M = molecular weight (g mol^{-1} and for magnetite 231.54 g mol^{-1}), N_A = 6.022 × 10^{23} mol^{-1} (Avogadro's number), z = unit cell number, in this case 8, and a = lattice parameter determined from XRD data.

$$\rho_{(XRD)} = \frac{M}{N_A} \times \frac{z}{a^3} \tag{21}$$

2.2.2. Longitudinal (V_L), shear (V_S), and mean (V_m) wave velocities

The respective longitudinal (V_L), shear (V_S), and mean (V_m) wave velocities are calculated from Eqs 22–24, respectively. Both stiffness parameters C_{11} and C_{44} are determined as discussed in the previous section.

$$V_L = \left(\frac{C_{11}}{\rho}\right)^{\frac{1}{2}} \tag{22}$$

$$V_S = \left(\frac{C_{44}}{\rho}\right)^{\frac{1}{2}} = \frac{V_L}{\sqrt{3}} \tag{23}$$

$$\frac{3}{V_m^3} = \frac{1}{V_L^3} + \frac{2}{V_S^3} \tag{24}$$

2.2.3. Longitudinal modulus, modulus of rigidity, bulk modulus, and Poisson's ratio

Once the wave velocity values V_L and V_S are determined, they can be used to determine other physical properties present in the sample material. The longitudinal modulus (L) can be determined using Eq 25, and the modulus of rigidity (G) can be determined using Eq 26 [51].

$$L = \rho \times (V_1)^2 \tag{25}$$

$$G = \rho \times (V_S)^2 \tag{26}$$

The values obtained from Eqs 25 and 26 can then be substituted into Eq 27 to determine Poisson's ratio.

$$\sigma = \frac{(L - 2G)}{2(L - G)} \tag{27}$$

In addition, the bulk modulus (B) of the sample is calculated using Eq 28 and the stiffness parameters C_{11} and C_{44} determined in the previous section.

$$B = \frac{1}{3} \times (C_{11} + 2C_{12}) \tag{28}$$

3. Materials and methods

3.1. Materials

Ferrous sulfate heptahydrate ($FeSO_4 \cdot 7H_2O$), ferric chloride ($FeCl_3$), and aqueous ammonia (NH_4OH, 28% w/w.) were purchased from Chem-Supply Pty Ltd, Australia. The analytical-grade ethanol used in the washing stages was supplied by Rowe Scientific Pty Ltd, Australia. All chemicals and solvents were used as supplied by the respective provider. All aqueous-based solutions prepared in this study were prepared using Milli-Q® water (18.3 M Ω cm^{-1}) generated by an ultrapure water system (Barnstead Ultrapure Water System D11931; Thermo Scientific, Dubuque, IA).

3.2. Preparation of BA leaf extract

A subset of healthy leaves was selected from BA plants located around the Murdoch University campus, Perth, Western Australia (32.0680° S, 115.8352° E). Selected leaves were thoroughly rinsed three times using Milli-Q® water to remove surface contaminants. Cleaned leaves were placed into a pre-heated oven at a temperature of 60 °C for 6 h to remove surface moisture. After the drying period, leaves were taken from the oven and individual leaves were cut into square (1 × 1 cm) pieces. From these leaf squares, 2 g was selected and placed into a glass beaker containing 100 mL of Milli-Q® water. This leaf-containing solution was heated to 80 °C and then maintained at this temperature for 120 min. During this period, the leaf-containing solution was constantly stirred, and the initial clear aqueous solution slowly changed to a yellow color. After 120 min, heat was removed and the solution containing the leaves and leaf extract was allowed to naturally cool down to room temperature (24 °C). Following the cooling period, the solution was filtered (Whatman® glass microfiber filters, Grade

GF/A) to remove the filtrate and produce the yellow-colored BA leaf extract solution (pH 5). The experimental procedure is schematically presented in Figure 1.

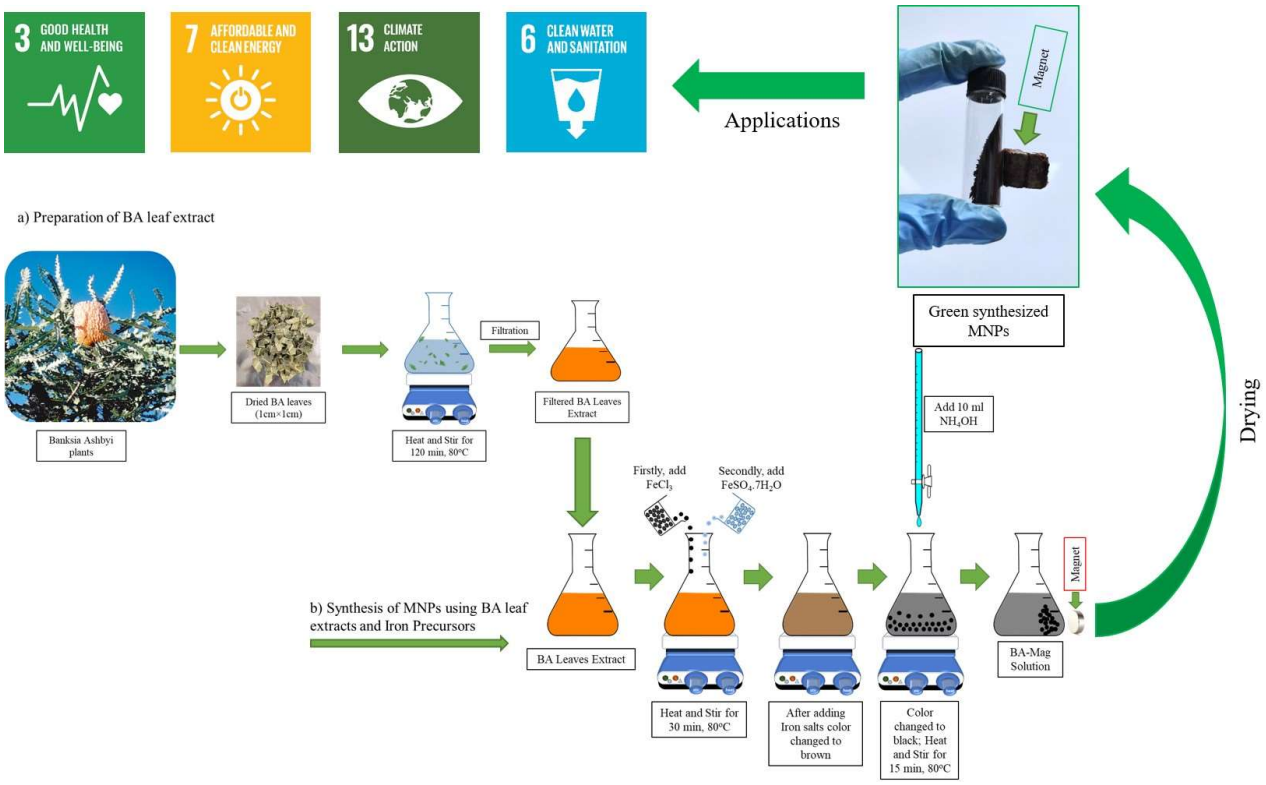

Figure 1. The overall biogenic procedure for producing MNPs from leaf extracts taken form BA.

3.3. Green synthesis of magnetite nanoparticles using BA leaf extract

Magnetite nanoparticles were synthesized using a co-precipitation method. Two types of nanoparticles were produced in individual 50 mL test solutions prepared in small flasks. The first type was the control and its starting solution was a 50 mL solution of Milli-Q® water. The magnetite nanoparticles produced in the aqueous solution were designated as MNPs. The second type of magnetite nanoparticles were created in a 50 mL solution of BA extract and these magnetite nanoparticles were designated as BA-MNPs. The test solutions were placed on a hotplate and heated to 80 °C. Next, $FeCl_3$ and $FeSO_4 \cdot 7H_2O$, in a molar ratio of 2:1, were added to each of the test solutions. The resulting reaction was then allowed to run for 30 min at 80 °C while being constantly stirred. During this period, the color of the BA extract solution changed from yellow to brown. At the end of the 30 min period, a 10 mL solution of NH_4OH (28% w/w.) was added dropwise to each test solution to increase the solution pH to between 11 and 12. After a further 15 min of stirring at 80 °C, a sizeable amount of black precipitate accumulated at the bottom of each flask. Then, both heating and stirring were stopped, and an external neodymium magnet was used to collect and remove the black precipitate from each of the test solutions. Before the respective black precipitates were vacuum-dried at 80 °C for 6 h, they were washed three times with Milli-Q® water and finally washed with an ethanol solution.

The overall reaction of the BA-assisted synthesis of MNPs is presented in Eq 29 below, and the experimental procedure is schematically presented in Figure 1.

$$\text{BA leaf extract} + Fe^{2+} + 2Fe^{3+} + 8OH^- \rightarrow (\text{BA-MNPs}) \text{ capped with phyto-molecules} + 4H_2O \quad (29)$$

3.4. Advanced characterization studies of the synthesized MNPs

X-ray diffraction was used to study the crystalline nature and particle size distribution of the samples using a Rigaku SmartLab X-ray diffractometer. The 2θ values were collected over the range 5–80°, with step angle increments of 0.01° and at a speed of 1°/min. The diffractometer used a Cu-Kα radiation source (λ = 1.5406 Å) and operated at 45 kV and 200 mA. Two electron microscopy studies were conducted to determine particle size, structural features, and morphology using a Zeiss Neon 40EsB FIBSEM located in the John de Laeter Center at Curtin University and a Philips CM200 TEM located at the FEG-TEM facility at Sophisticated Analytical Instrument Facility (SAIF), Indian Institute of Technology, Mumbai (India), for high-resolution images. In addition, the Zeiss Neon also used its energy dispersive spectroscopy (EDS) attachment to determine the compositional analysis of the samples and the Philips CM200 also provided selected area electron diffraction (SAED) patterns of the samples. For the Zeiss Neon, samples were deposited on carbon tape-covered SEM holders and then sputter coated (E5000, Polaron Equipment Ltd.) with a 2 nm thick layer of platinum to prevent charge build-up. Samples for the Philips CM200 TEM were prepared by placing the samples on a carbon-coated TEM support grid (copper) and then sputter-coated with a 10 nm thick layer of gold to prevent charge build-up. A PerkinElmer FT-IR/NIR Spectrometer Frontier fitted with a universal signal bounce Diamond ATR attachment was used to carry out an FT-IR study of the samples to identify the various functional groups present. The analysis was carried out over the wavenumber interval between 400 and 4000 cm^{-1}, with a wavenumber resolution step of 1 cm^{-1}. Raman spectroscopy was used to determine the molecular vibrations and chemical compositions of the various samples. Measurements were made using a LabRAM 1B Raman spectrometer that used a 632.82 nm Helium-Neon laser light source. Analysis was carried out over the wavenumber interval between 0 and 3000 cm^{-1}, with a wavenumber resolution step of 1 cm^{-1}. UV-vis was carried out using a Perkin Elmer STA 8000 spectrometer over a spectral range between 300 and 1100 nm, with a range resolution of 1 nm. TGA was conducted to evaluate the thermal stability of the respective samples using a Perkin Elmer simultaneous thermal analyzer STA 8000. Samples were placed into a ceramic (Alumina) crucible and loaded into the STA 8000. Thermal stability analysis was conducted with an airflow rate of 20 mL min^{-1} and over a temperature range between 30 and 800 °C, with an incremental heating rate of 25 °C min^{-1}.

4. Results and discussion

4.1. X-ray diffraction measurements

XRD analysis was used to identify crystallographic structures and phase purity of the synthesized control MNPs and BA-MNPs. XRD spectra of the respective samples are presented in Figure 2a. Inspection of Figure 2a reveals six significant diffraction peaks occurring at 2θ locations of 30.46, 35.78, 43.46, 53.88, 57.48, and 63.08°. These peaks were indexed and found to conform to

the Miller indices of (220), (311), (400), (422), (511), and (440) crystal planes, respectively. These peaks are in good agreement with the standard card pattern (JCPDS No. 19-629) for pure Fe_3O_4 nanoparticles and correspond to a cubic structure with a space group of Fd-3m [52,53]. The diffraction patterns also confirm there were no other impurities present and indicate the capping agents were effective in preventing atmospheric oxidation.

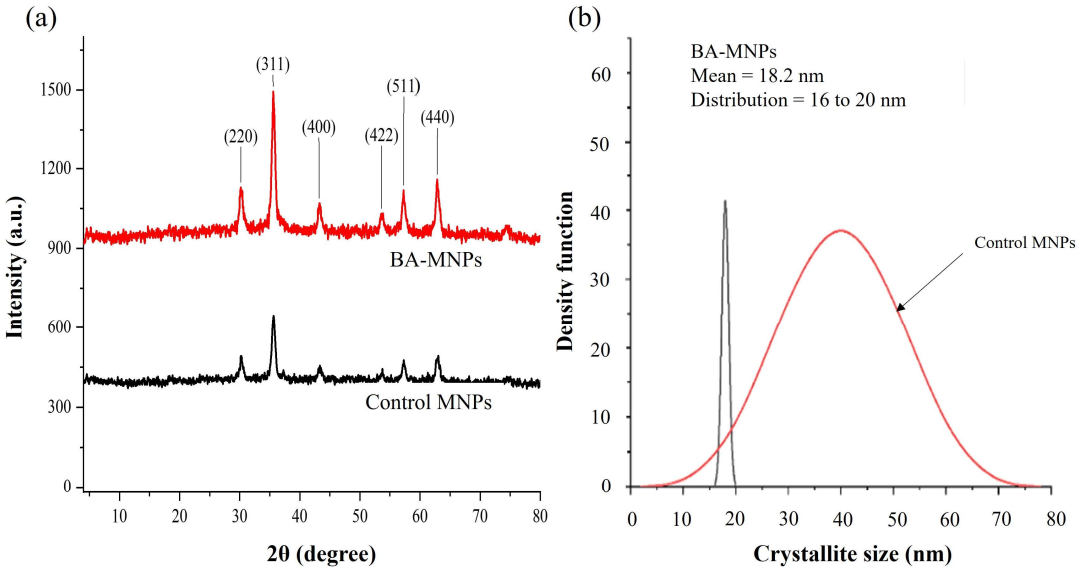

Figure 2. (a) Representative XRD patterns of control MNPs and BA-MNPs and (b) particle size distribution of control MNPs and BA-MNPs.

Analysis of the XRD data revealed the BA-assisted synthesis process produced BA-MNPs with a smaller crystallite size. Table 1 presents the results of the crystallite size and crystallite size distribution study. Inspecting both Figure 2b and Table 1 reveals that both the size and size distribution of the BA-MNPs were smaller than the control MNPs produced without the presence of BA extract. Importantly, the crystallite size distribution of the BA-MNPs was very narrow when compared to the control MNPs. The narrow range between 16 and 20 nm of the BA-MNPs shows that the presence of BA extract in the synthesis process acts as a nanoparticle size regulator.

Table 1. Crystallite size and size distribution of synthesized control MNPs and BA-MNPs.

Sample	Scherrer (nm)	Rigaku SmartLab XRD	
		Size (nm)	Size distribution (nm)
Control MNPs	38	40	5–75
BA-MNPs	16.03	18.2	16–20

4.2. X-ray peak profile analysis using Williamson-Hall methods

The XRD data was first analyzed using the uniform deformation model (UDM) that was presented in Eq 9. Then, by plotting 4 sinθ along the x-axis and $\beta_{(hkl)}$ cosθ along the y-axis, a linear relationship was established, as seen in Figure 3a. From the graphical analysis, the micro-strain (slope) was found to be -2.6×10^{-3} and indicated the sample was under compression. The crystallite size determined

from the y-intercept was found to be 9.11 nm, smaller than the Scherrer value of 38 nm. The second analysis method used the uniform stress deformation model (USDM) presented in Eq 11. The respective mechanical compliances for the BA-MNPs were determined and summarized in Table 2. The compliances were then used to determine the respective elastic modulus $E_{(hkl)}$ for each crystallographic plane, as seen in Table 3. Then, by plotting $4\sin\theta/E_{(hkl)}$ along the x-axis and $\beta_{(hkl)} \cos\theta$ along the y-axis, a linear relationship was established, as seen in Figure 3b.

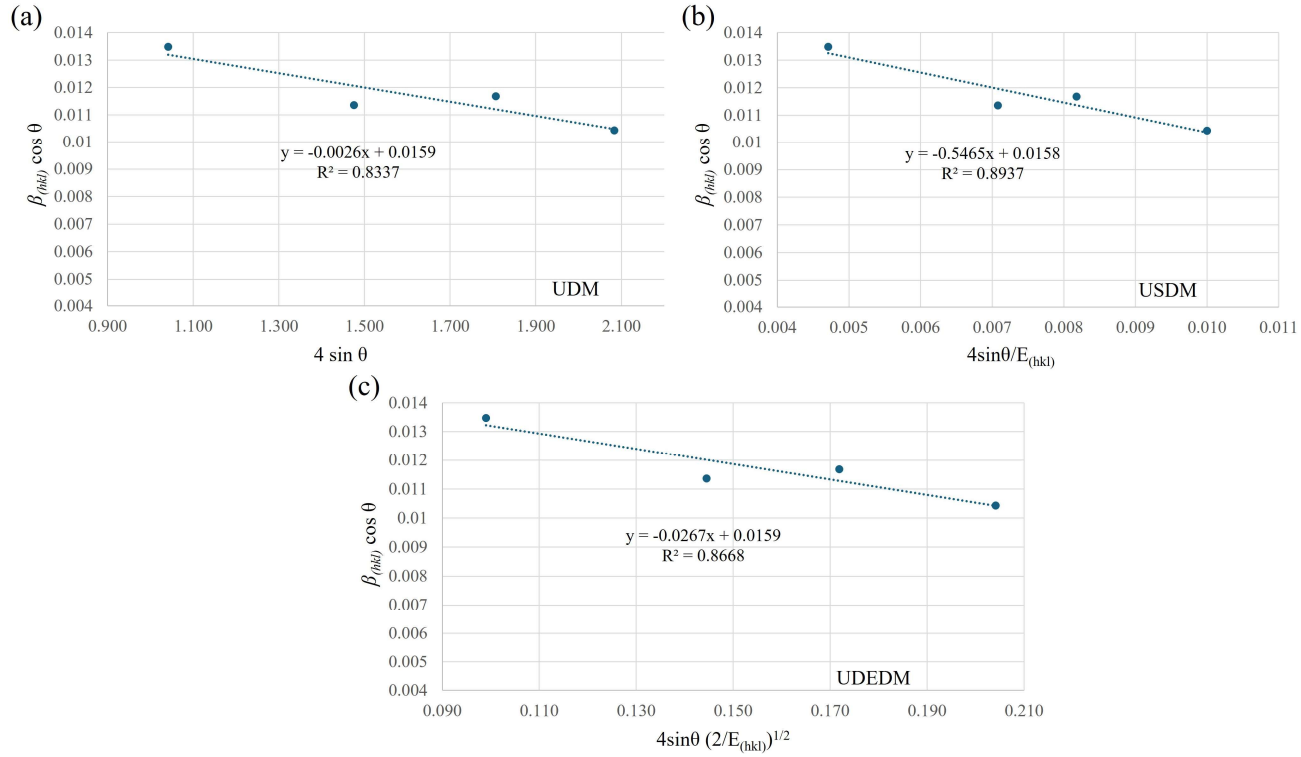

Figure 3. (a) UDM, (b) USDM, and (c) UDEDM plots of synthesized BA-MNPs.

Table 2. Mechanical compliance values for the synthesized BA-MNPs [54].

Material property	Value	
Elastic compliances	S_{11}	4.80×10^{-12} Pa^{-1}
	S_{12}	-1.37×10^{-12} Pa^{-1}
	S_{44}	10.13×10^{-12} Pa^{-1}
Stiffness parameters	C_{11}	270 GPa
	C_{12}	108 GPa
	C_{44}	98.7 GPa

Table 3. Modulus of elasticity for each crystal orientation in the synthesized BA-MNPs.

Crystal orientation	Modulus of elasticity, E (GPa)
{220}	221.06
{311}	225.49
{400}	208.33
{422}	220.94
{511}	220.44

From the graphical analysis, the stress was found to be −546.5 MPa, indicating the stress was compressive in nature. The micro-strain was estimated to be -2.47×10^{-3}, and the crystallite size was found to be 9.17 nm. The third analysis method used the UDEDM presented in Eq 20. In this analysis, the UDEDM considers the influence of the strain energy density (u), which was calculated using Eq 19 and then substituted into Eq 20. Then, by plotting $4sin\theta\ (2/E_{(hkl)})^{1/2}$ along the x-axis and $\beta_{(hkl)}cos\theta$ along the y-axis, a linear relationship was established, as seen in Figure 3c. From the graphical analysis, the energy density was found to be 710 KJ/m^3, and the micro-strain was estimated to be -2.54×10^{-3}. The analysis also found the crystallite size was 9.11 nm. The results of the three models are summarized in Table 4.

Table 4. Summary X-ray peak profile analysis using Williamson-Hall methods.

Sample	UDM		USDM			UDEDM			Average E (GPa)
BA-MNP	$D_{(hkl)}$ mm	Strain ε (10^{-3})	$D_{(hkl)}$ mm	Stress σ (MPa)	Strain ε (10^{-3})	$D_{(hkl)}$ mm	Energy density (KJ/m^3)	Strain ε (10^{-3})	
	9.11	−2.60	9.17	−546.5	−2.47	9.11	710	−2.54	217.44

Table 5. Size comparison between other studies using a chemical synthesis method to generate MNPs.

Researcher	Average crystallite size $D_{(hkl)}$ (nm)	References
Chaki, S.H., et al. (2015)	6.58	[55]
Yusoff, A.H.M., et al. (2017)	8–28	[56]
Kushwaha, P., et al. (2021)	13–18	[57]
Ilyas, S., et al. (2019)	22.5	[58]
Control sample	5–75	This study
Williamson-Hall modeling	Mean 9.13	This study
Debye-Scherrer method	16.03	This study
Rigaku SmartLab FP analysis	18.20	This study

The $D_{(hkl)}$ value of the BA-MNPs estimated using the Debye-Scherrer equation was found to be 16.03 nm, slightly smaller than the 18.02 nm determined by the Rigaku SmartLab FP analysis. The $D_{(hkl)}$ values determined from UDM, UDSM, and UDEDM models are consistent with each other, as seen in Table 4. The mean $D_{(hkl)}$ value of 9.13 nm determined from these models is also consistent with the values obtained using the Debye-Scherrer method and Rigaku SmartLab FP analysis. Importantly, these sizes are comparable to those obtained by other researchers producing magnetite nanoparticles

using similar chemical precipitation techniques, as seen in Table 5. In addition, the UDM, UDSM, and UDEDM models also give consistent negative lattice micro-strain values, thus indicating that the BA-MNPs are experiencing compressive stress and explaining the peak broadening seen in the XRD data [47]. Significantly, the presence of strain, whether compressive or tensile, often leads to peak broadening and even displacement of the 2θ peak position [59]. In addition, the synthesis technique itself contributes to the micro-strain experienced by the formed nanoparticles. For instance, during planetary ball-milling, nanoparticles experience high stresses, and the high residual stress generates large micro-strains [60]. Less stress-inducing chemical synthesis techniques like the co-precipitation method used in this study produce lower micro-strains in the generated MNPs [61,62].

4.3. Physical properties determined from XRD data

Data derived from the XRD diffraction pattern was used to determine the lattice parameter (a), as presented in Eq 4; the lattice volume (V) was calculated using Eq 5, as detailed in section 2. Then, the lattice parameter value was used to calculate the sample density $\rho_{(XRD)}$ using Eq 21. The calculated values for a, V, and $\rho_{(XRD)}$ are presented in Table 6.

Table 6. Lattice constant, unit cell volume, and XRD derived density of synthesized BA-MNPs.

Sample	Lattice constant a (Å)	Unit-cell volume V (Å^3)	$\rho_{(XRD)}$ (gcm^{-3})
BA-MNPs	8.362	584.696	5.260

Once the $\rho_{(XRD)}$ was calculated, its value was substituted into Eqs 22–24 to calculate the longitudinal (V_L), shear (V_S), and mean (V_m) wave velocities, respectively. The calculated values for the respective wave velocities are presented in Table 7. Next, the wave velocity values of V_L and V_S were used to determine the longitudinal modulus (L) and the modulus of rigidity (G) using Eqs 25 and 26, respectively. Then, the longitudinal modulus and modulus of rigidity values were substituted into Eq 27 to calculate Poisson's ratio (σ). The calculated value of Poisson's ratio was found to be 0.2354, within the range between –0.9 and 0.5, which is consistent with the theory of isotropic elasticity. Finally, the bulk modulus of the sample was calculated using Eq 28. The values obtained in this study are similar to those derived by other researchers investigating the properties of magnetite nanoparticles [63,64]. The various calculated values, such as wave velocities, moduli, and Poisson's ratio, are summarized in Table 7.

Table 7. Physical properties of synthesized BA-MNPs determined from XRD data.

Sample	$\rho_{(XRD)}$ (gcm^{-3})	V_L (ms^{-1})	V_S (ms^{-1})	V_m (ms^{-1})	L (GPa)	G (GPa)	σ	B (GPa)
BA-MNPs	5.260	7164.5	4136.4	4592.2	270.01	89.98	0.2354	159.87

4.4. FIBSEM and TEM microscopy studies

4.4.1. FIBSEM microscopy study

The size, chemical composition, and morphology of the BA-MNPs produced in this study were characterized using a Zeiss Neon 40EsB FIBSEM and a Philips CM200 TEM. Inspection of the FIBSEM image presented in Figure 4a reveals that the synthesized BA-MNPs are highly agglomerated and need ultrasonic treatment to break up the large nanoparticle clusters [65]. Analysis of the FIBSEM images presented in Figure 4b also reveals the BA-MNPs have a spherical geometry with a mean diameter of 18 ± 5 nm. This size range is similar to the size estimates of 16.03 and 18.2 nm produced by the Scherrer method and the Rigaku SmartLab, respectively. In addition, the ±5 nm limits of the particle diameter also confirm the results of the Rigaku SmartLab analysis, which gave a size distribution range between 16 and 20 nm. Moreover, an EDS analysis was performed to confirm the formation and elemental composition of the BA-MNPs, as seen clearly in Figure 4c. Inspection of the EDS analysis reveals two strong Fe peaks located at 0.7 and 6.4 KeV, and a less pronounced Fe peak located at 7.1 KeV. Moreover, there is an intense peak located at 0.4 KeV, which represents the presence of oxygen. No other elements were detected in the EDS analysis. Thus, the ratio between Fe and O signals confirms the synthesized nanoparticles are indeed magnetite [66].

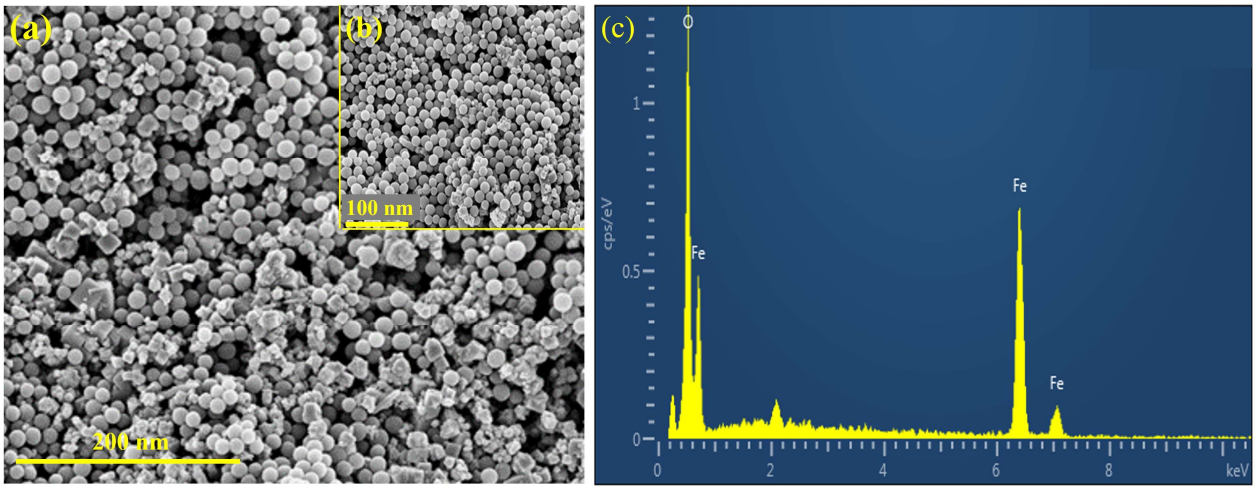

Figure 4. FIBSEM images of BA-MNPs. (a and b) showing spherical morphology and (c) EDS elemental analysis confirming BA-MNPs formation.

4.4.2. TEM microscopy study

Figure 5 presents the results of the TEM investigation. Inspection of Figure 5a,b confirms the particle size and shape seen in the FIBSEM images presented in Figure 4. The images also confirm the tendency of the BA-MNPs to agglomerate. The agglomeration of the BA-MNPs can be attributed to the effects of van der Waals forces that facilitate nanoparticle attraction and clustering. Moreover, it is worth noting that the BA leaf extract contains the O–H functional group that has the potential to induce agglomeration [67]. In addition, SAED pattern analysis and high-resolution TEM image analysis was carried out to determine lattice plane spacing. Figure 5c shows the SAED pattern for the BA-MNPs

sample. The diffraction rings were successfully indexed as (311), (220), (400), (422), (511), and (440). The indexing agreed with the XRD analysis, and similar results have been reported in the literature for magnetite nanoparticles [59,68]. The high-resolution TEM image shown in Figure 5d confirms the nanometer-scale polycrystalline structure of the BA-MNPs. The image analysis also found that the lattice spacing planar distance was 0.22 nm, confirming the results of the XRD data. Both the SAED pattern data and high-resolution image analysis confirm the well-defined crystalline structure of the BA-MNPs.

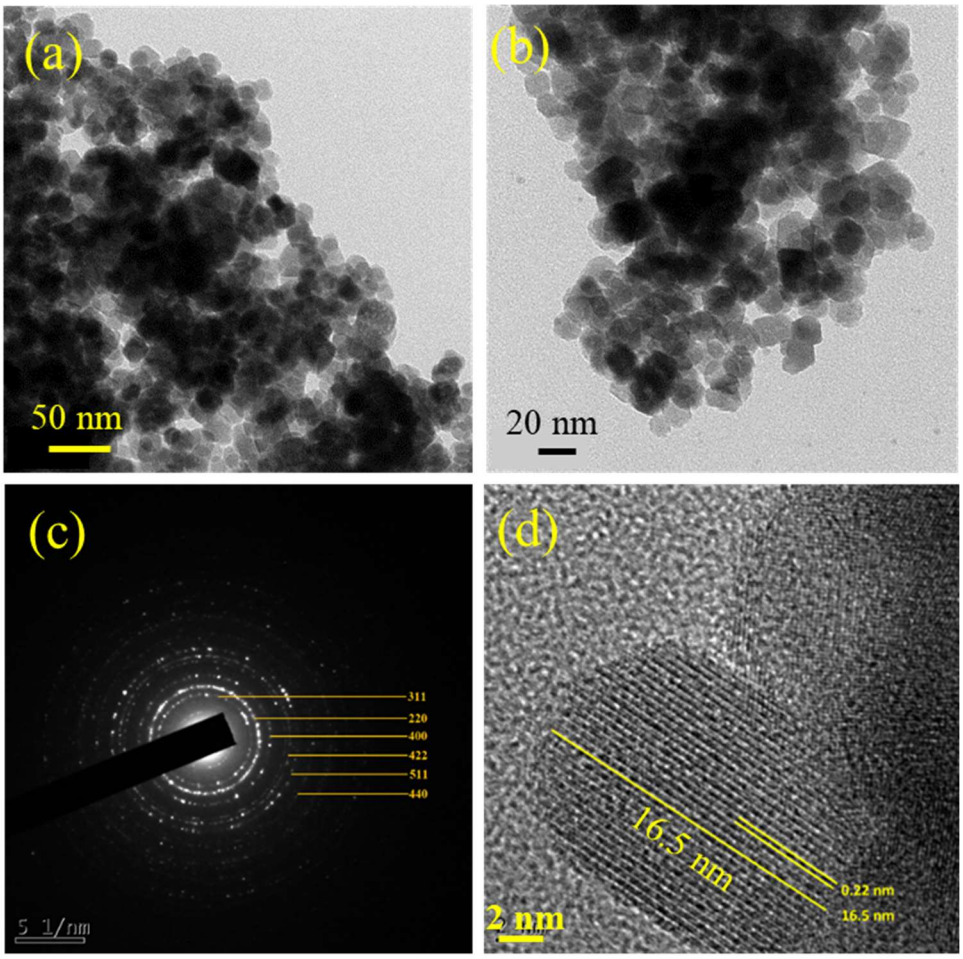

Figure 5. TEM images (a and b) of the BA-MNPs showing their size and structure, (c) SAED pattern, and (d) high-resolution image showing nanometer scale polycrystalline structure of the BA-MNPs.

4.5. Fourier-transform infrared and Raman spectroscopy

4.5.1. FT-IR spectroscopy study

All the functional groups present in the BA extract and BA-MNPs were studied by FT-IR. Figure 6a shows a representative spectrum of each sample. The upper spectra in Figure 6a is the BA extract and shows bands located at 3357, 2918, 2849, 1731, 1604, 1516, 1161, and 1032 cm^{-1}. The presence of these bands in the BA extract indicates the presence of flavonoids and phenolic functional groups in

the BA extract, which have the potential to initially reduce metal ions to form metal nanoparticles and then stabilize the formed nanoparticles. A broad band was observed at 3357 cm^{-1} and was attributed to O–H stretching. Bands located at 2918 and 2849 cm^{-1} were assigned to C–H asymmetric and symmetric stretching vibrations of the methyl group. The band located at 1731 cm^{-1} was assigned to C=O stretching, and 1604 cm^{-1} was attributed to C–O vibrations. The band the located at 1516 cm^{-1} was assigned to Amide II linkage, and bands 1161 and 1032 cm^{-1} where attributed to coupled C–C and C–O vibrations of the phenolic group. The respective bands and assigned functional groups are summarized in Table 8.

Table 8. Summary of characteristic FT-IR absorption bands and functional groups seen in FT-IR spectra for BA extract and BA-MNPs.

Wavelength (cm^{-1})	Functional group	References
3000–3600	O–H functional group of phenol from BA-Raw	[69]
2918, 2849	C–H asymmetric and symmetric stretching vibrations of the methyl group	[70]
1731	C=O stretching due to xylan in hemicellulose	[71]
1631	C=O group of carboxylic acid	[72]
1604	C–O/aromatic C–C stretching	[73]
1516	Amide II linkage	[74]
1432	Asymmetric and symmetric vibration of COO–	[74]
1400–1466	H–C–H bending vibrations	[75]
551	Fe–O bond vibration	[75]
1000–1350	Coupled C–C and C–O vibrations of the phenolic group	[76]

The lower spectrum in Figure 6a is the BA-MNP sample and shows bands located at 3408, 1631, 1432, 1105, and 551 cm^{-1}. The band located at 3408 cm^{-1} was attributed to O–H stretching and was shifted from 3357 cm^{-1} in the BA extract spectra. The shift suggests that the O–H functional group is acting as a reducing agent during the synthesis of the BA-MNPs [72,77,78]. The band located at 1631 cm^{-1} is believed to be the C=O group of carboxylic acid, which represents the carboxyl functional group (–COOH), with a slightly increased magnitude. The increase in magnitude of the band suggests the carboxyl functional group is acting as a capping agent during the formation of the BA-MNPs [78]. The band located at 1432 cm^{-1} was assigned to the asymmetric and symmetric vibration of COO–, while the band located at 1105 cm^{-1} was assigned to the C–O stretching vibration of phenolic groups. The final band in the spectra is located at 551 cm^{-1} and is assigned to Fe–O (stretching vibration) and confirms the formation of MNPs [72, 79–81]. The respective bands and assigned functional groups are summarized in Table 8.

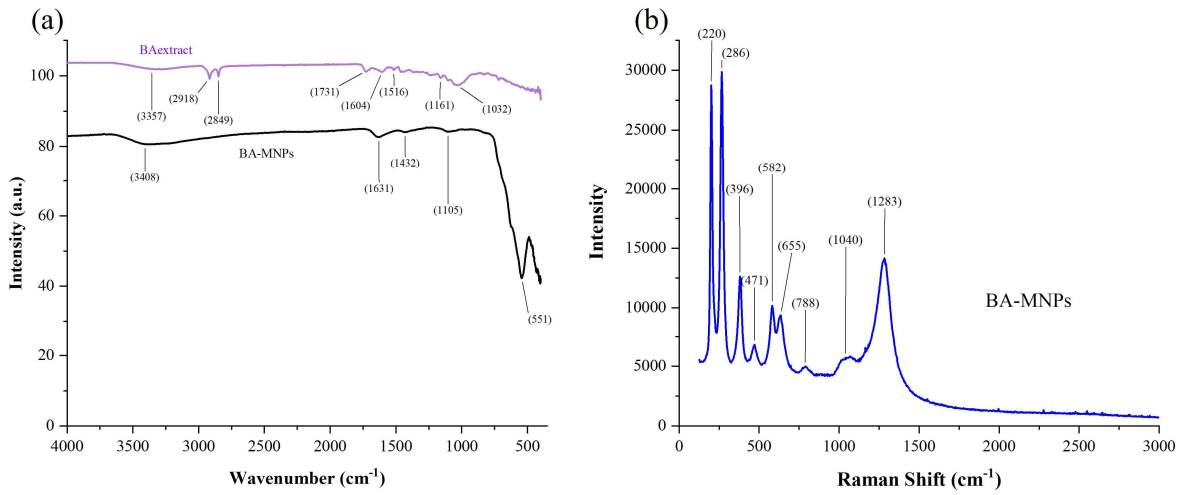

Figure 6. (a) FT-IR spectra of raw BA extract and BA-MNP samples and (b) Raman spectrum of BA-MNP sample.

4.5.2. Raman spectroscopy study

Figure 6b shows a representative Raman spectrum of a BA-MNP sample. The spectrum shows a strong peak located at 1283 cm^{-1}, identified as the D-band of the BA-MNPs. The four peaks seen at 396, 471, 582, and 6555 cm^{-1} correspond to the vibration modes of the Fe–O bonds present in the BA-MNPs [82,83]. Also present are two strong peaks located at 220 and 286 cm^{-1}, which were the result of an oxidation reaction that occurred during the Raman spectroscopy procedure [84]. Moreover, peaks located at 788 and 1040 cm^{-1} suggest organic compounds have induced surface modifications on the BA-MNPs. This result suggests the phytochemicals present in the BA extract can influence surface functionalization processes on the BA-MNPs [85,86]. Overall, the Raman spectrum is similar to other Raman studies reported in the literature and also confirms the formation of BA-MNPs [87].

4.6. UV-VIS spectroscopy and thermo-gravimetric analysis

4.6.1. UV-VIS spectroscopy study

A UV-visible spectrum of a representative BA-MNP sample is presented in Figure 7a. The spectra show a wide absorption range between 300 and 800 nm. However, there is a significant region of absorbance between 350 and 450 nm [88]. The absorption band in the UV range between 330 and 450 nm confirms the formation of BA-MNPs and is similar to reports discussed in the literature for plant-synthesized magnetite nanoparticles [89,90]. In addition, the UV-visible data was used to calculate the direct optical band-gap energy (Eg) for the BA-MNPs using Tauc's equation below:

$$\alpha h\nu = K\left(h\nu - E_g\right)^n \tag{30}$$

In Eq 30, α = absorption coefficient, $h\nu$ = incident photon energy, B is a material-dependent constant, E_g = optical band gap in electron-volts (eV), and n = an exponent that can take different values depending on the nature of the electronic transition. When the data from Eq 30 was plotted graphically with $h\nu$ along the x-axis and $\alpha h\nu^2$ along the y-axis, the Tauc curve was produced, as seen

in Figure 7b. Interception of the extrapolated linear part of the curve with the x-axis gave a band gap value of 2.63 eV. This band gap value is similar to those reported in the literature for magnetite nanoparticles synthesized by plants [88–91].

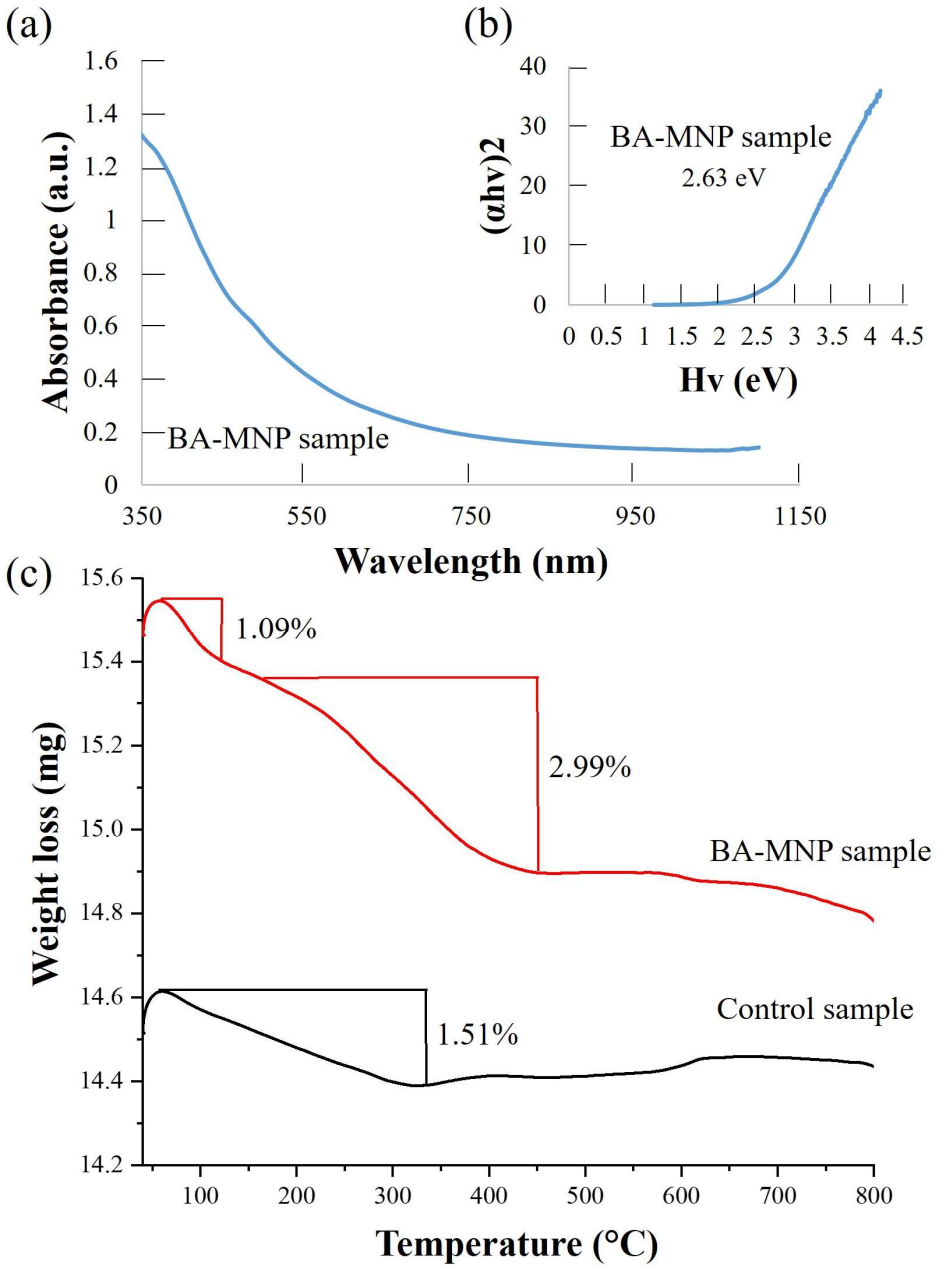

Figure 7. UV-VIS spectroscopy analysis of BA-MNP sample: (a) UV-VIS spectrum investigated in the study, (b) calculation of BA-MNP band gap energy, and (c) TGA analysis of control MNPs and BA-MNPs.

4.6.2. Thermo-gravimetric analysis

The results of TGA studies of the control MNPs and the BA-MNPs are presented in Figure 7c. Analysis of the control MNPs shows a steady decrease in sample weight of around 1.51% between 24 and 330 °C. During the early part of this stage, water present in the capping vaporizes, leaving the

salt-based capping still attached to the surface of the MNPs. However, at around 330 °C, the salt-based coating has decomposed, leaving the bare MNPs. After 330 °C, a small increase in weight occurs as the temperature and time increase. This small increase in weight was caused by the control MNPs undergoing surface oxidation [92]. TGA analysis of the BA-MNPs shows a two-step decomposition process over the temperature range, as seen in Figure 7c. During the first stage, between 24 and 120 °C, there was a weight loss of 1.09% due to water evaporation and decomposition of some volatile phytochemicals [93,94]. During the second stage, between 150 and 400 °C, there was a further weight loss of 2.99%. During this stage, salts and phytochemicals on the surface of the nanoparticles decomposed until only bare MNPs remained [95–97]. Overall, the thermal studies have shown the nanoparticle capping starts to decompose around 100 °C; by 400 °C, the capping agent was no longer present on the surface of the BA-MNPs.

4.7. Life cycle assessment and cost analysis

4.7.1. Life cycle assessment (LCA) of the BA-MNPs

LCA analysis was used to assess the environmental impact of the BA-MNPs produced in this study. The LCA analysis adhered to the procedures and guidelines as specified in ISO14040:2006 and ISO14044:2006 [98,99]. Table 9 presents a complete list of items used in preparing BA-MNPs.

Table 9. Inventory data needed to conduct an LCA analysis for the preparation of BA-MNPs from BA leaf extract.

Material/Process	Unit	Input
Transportation	t-km	0
Transportation of BA leaves	t-km	0
Preparation of BA leaf extract	-	-
BA leaves	g	2
Milli-Q® water for cleaning BA leaves	mL	100
Electrical energy for drying leaves	MJ	0.04
Deionized water for supernatant	mL	100
Electrical energy for heating	MJ	2.29
BA-Mag NPs synthesis	-	-
$FeCl_3$	g	1.33
$FeSO_4 \cdot 7H_2O$	g	0.67
Electrical energy for heating	MJ	0.72
NH_4OH (28%)	g	0.01
Ethanol for cleaning	mL	50
Milli-Q® water for cleaning	mL	200
Electrical energy for vacuum drying	MJ	0.72
Total energy use	MJ	13.99
Total water use	mL	400

The life cycle inventory (LCI) for producing BA-MNPs from BA leaf extract was developed by deconstructing process inputs and emissions, as shown in Table 10. The procedure uses Eco-Invent datasets to model the environmental impact associated with the production and consumption of each input.

Table 10. Summary of LCI inputs needed to prepare BA-MNPs from BA leaf extract.

Category	Unit	Total	CO_2 emissions
Total water use	mL	400	N/A
Total energy use	MJ	3.77	0.0784 kg CO_2
Total CO_2 emissions	kg	-	0.0784 kg CO_2

From the LCI analysis, the overall CO_2 emissions for the complete process were 0.0784 kg. The CO_2 was generated from the energy needed for experimental processes like heating and vacuum drying and the production of precursor materials like $FeCl_3$ and $FeSO_4 \cdot 7H_2O$. In terms of CO_2 emissions, the production of $FeCl_3$, $FeSO_4 \cdot 7H_2O$, ethanol, and NH_4OH are minimal.

4.7.2. Cost analysis of producing BA-MNPs

An assessment of the costs associated with new nanoparticle-based products is essential for determining their viability in transitioning from laboratory-based exploratory projects to pilot-based studies and then to large-scale industrial manufacturing for specific commercial applications [100]. The present cost analysis assesses the financial feasibility of the experimental procedure for producing BA-MNPs. Thus, a comprehensive analysis of the critical elements affecting the cost of production is crucial and needs to take in several factors, including: (1) availability of raw materials; (2) processing conditions and protocols; (3) processing equipment; (4) transportation; (5) labor; and (6) operational costs. In the context of the present exploratory study, the precursor BA leaves were readily available, other precursor material costs were negligible, and processing the BA-MNPs at the laboratory scale was straightforward and used standard in-house equipment. Therefore, the following analysis considers the driving expenses associated with synthesizing BA-MNPs. These expenses were determined through Eq 31.

$$\text{BA-MNPs production cost} = DC + HC + VDC \tag{31}$$

In Eq 31, DC is the cost of drying samples after initial cleaning, HC is the heating cost during processing, and VDC is the vacuum drying cost after initial nanoparticle synthesis. Thus, the major expenses associated with BA-MNP production were drying, heating, and vacuum drying. The cost of each energy consumption activity was calculated using Eq 32.

$$\text{Activity cost} = \text{Time (h)} \times \text{Equipment Power (kW)} \times \text{electricity tariff in Australia} \tag{32}$$

Other cost items are listed in Table 11. Inspection of Table 11 reveals the cost of producing BA-MNPs in this exploratory study was 1.26 USD/kg.

Table 11. Estimated cost for producing 1 kg of BA-MNPs.

BA-Mag NPs synthesizing steps	Cost ($/kg)
BA-MNP production cost ($D_C + H_C + VD_C$)	0.78
Cost of $FeCl_3$ (IG)*	0.14
Cost of $FeSO_4 \cdot 7H_2O$ (IG)*	0.10
Cost of NH_4OH (28%)	0.01
Cost of EtOH	0.23
Total cost	1.26

**IG is the estimated cost of chemicals (www.chemsupply.com.au & www.sigmaaldrich.com).

5. Conclusions

This exploratory study established that the Australian indigenous plant BA could be used in a co-precipitation method involving $FeCl_3$ and $FeSO_4 \cdot 7H_2O$ to regulate the size and size distribution of the synthesized BA-MNPs. The mean particle size of the BA-MNPs was found to be 18.2 nm, and the narrow size distribution ranged from 16 to 20 nm. X-ray peak profile analysis using the UDM, USDM, and UDEDM models found the average crystallite size to be 9.13 nm. All the models showed that the crystal lattice of the BA-MNPs experienced a compressive stress of around 546 MPa. The models also found the BA-MNPs experienced an average micro-strain of 2.54×10^{-3}. The study also used the XRD data to determine material properties, such as density (5.260 kg/m^3), average Young's modulus of elasticity (217 GPa), and modulus of rigidity (90 GPa). Both FIBSEM and TEM microscopy studies confirmed the crystalline nature of the BA-MNPs and their size range. FT-IR and Raman spectroscopy verified the purity of the BA-MNPs and confirmed that the phytochemicals present in the BA extract acted as both reducing and capping agents. TGA analysis found the BA-MNPs were thermally stable over a temperature range of 24–800 °C, with the capping decomposing at around 400 °C. The laboratory cost for producing the BA-MNPs was found to be 1.26 USD/kg, and the overall emission of CO_2 during the synthesis process was 0.0784 kg. Overall, the results show the co-precipitation method, using BA leaf extracts as a particle size regulator, can produce highly stable and pure BA-MNPs within a narrow size distribution. Future work will involve scaling up the current experimental procedure to produce commercial quantities of BA-MNPs. Future work will also involve refining the experimental procedure to tailor the properties of the BA-MNPs for specific applications, such as photocatalysts, bio-sensing and diagnosis carriers in medicine, and components in electronic and data storage devices.

Use of AI tools declaration

The authors declare they have not used Artificial Intelligence (AI) tools in the creation of this article.

Acknowledgments

Mr. A F M Fahad Halim would like to thank Murdoch University, Australia, for a scholarship to undertake his PhD studies. The authors would like to thank Mrs. Elaine Miller at the John de Laeter Center located at Curtin University for her assistance with FIBSEM imaging and the FEG-TEM facility

located at Sophisticated Analytical Instrument Facility (SAIF), Indian Institute of Technology, Mumbai (Bombay), for their assistance with TEM microscopy.

Author contributions

Gerrad Eddy Jai Poinern conceived and planned the experiments, manuscript drafting, and proofreading. A F M Fahad Halim carried out the synthesis experiments, characterizations, data collection, literature search, manuscript drafting, and WH analysis. Derek Fawcett contributed to the interpretation of the results, manuscript drafting, literature search, and editing. Peter Chapman carried out the Raman spectroscopy. Rupam Sharma was involved in the TEM investigations. All authors provided critical feedback and helped shape the research, analysis, and manuscript final preparations.

Conflict of interest

The authors declare no conflict of interest.

References

1. Ahmadi S, Chia CH, Zakaria S, et al. (2012) Synthesis of Fe_3O_4 nanocrystals using hydrothermal approach. *J Magn Magn Mater* 324: 4147–4150. https://doi.org/10.1016/j.jmmm.2012.07.023
2. Montoro VNCE (1938) Miscibilita fra gli ossidi salini di ferro e di manganese. *Gaz Chim Ital* 68: 728–733.
3. Cotar AI, Grumezescu AM, Huang KS, et al. (2013) Magnetite nanoparticles influence the efficacy of antibiotics against biofilm embedded *Staphylococcus aureus* cells. *Biointerface Res Appl Chem* 3: 559–565. Available from: http://grumezescu.com/?corpo_portfolio=magnetite-nanoparticles-influence-the-efficacy-of-antibiotics-against-biofilm-embeddedstaphylococcus-aureus-cells.
4. Gu T, Zhang Y, Khan SA, et al. (2019) Continuous flow synthesis of superparamagnetic nanoparticles in reverse miniemulsion systems. *Colloid Interface Sci Commun* 28: 1–4. https://doi.org/10.1016/j.colcom.2018.10.005
5. Ma J, Lee SMY, Yi C, et al. (2017) Controllable synthesis of functional nanoparticles by microfluidic platforms for biomedical applications—A review. *Lab Chip* 17: 209–226. https://doi.org/10.1039/C6LC01049K
6. Mohammadi H, Nekobahr E, Akhtari J, et al. (2021) Synthesis and characterization of magnetite nanoparticles by co-precipitation method coated with biocompatible compounds and evaluation of in-vitro cytotoxicity. *Toxicol Rep* 8: 331–336. https://doi.org/10.1016/j.toxrep.2021.01.012
7. Soleymani M, Khalighfard S, Khodayari S, et al. (2020) Effects of multiple injections on the efficacy and cytotoxicity of folate-targeted magnetite nanoparticles as theranostic agents for MRI detection and magnetic hyperthermia therapy of tumor cells. *Sci Rep* 10: 1695. https://doi.org/10.1038/s41598-020-58605-3
8. Chircov C, Grumezescu AM, Holban AM (2019) Magnetic particles for advanced molecular diagnosis. *Materials* 12: 2158. https://doi.org/10.3390/ma12132158

9. López YC, Antuch M (2020) Morphology control in the plant-mediated synthesis of magnetite nanoparticles. *Curr Opin Green Sustainable Chem* 24: 32–37. https://doi.org/10.1016/j.cogsc.2020.02.001
10. Zhao CX, He L, Qiao SZ, et al. (2011) Nanoparticle synthesis in microreactors. *Chem Eng Sci* 66: 1463–1479. https://doi.org/10.1016/j.ces.2010.08.039
11. Ficai D, Grumezescu V, Fufă OM, et al. (2018) Antibiofilm coatings based on PLGA and nanostructured cefepime-functionalized magnetite. *Nanomaterials* 8: 633. https://doi.org/10.3390/nano8090633
12. Sirivat A, Paradee N (2019) Facile synthesis of gelatin-coated Fe_3O_4 nanoparticle: Effect of pH in single-step co-precipitation for cancer drug loading. *Mater Design* 181: 107942. https://doi.org/10.1016/j.matdes.2019.107942
13. Taufiq A, Nikmah A, Hidayat A, et al. (2020) Synthesis of magnetite/silica nanocomposites from natural sand to create a drug delivery vehicle. *Heliyon* 6: e03784. https://doi.org/10.1016/j.heliyon.2020.e03784
14. Ladole MR, Pokale PB, Patil SS, et al. (2020) Laccase immobilized peroxidase mimicking magnetic metal organic frameworks for industrial dye degradation. *Bioresour Technol* 317: 124035. https://doi.org/10.1016/j.biortech.2020.124035
15. De Queiroz DF, de Camargo ER, Martines MU (2020) Synthesis and characterization of magnetic nanoparticles of cobalt ferrite coated with silica. *Biointerface Res Appl Chem* 10: 4908–4913. https://doi.org/10.33263/BRIAC101.908913
16. Gao G, Liu X, Shi R, et al. (2010) Shape-controlled synthesis and magnetic properties of monodisperse Fe_3O_4 nanocubes. *Crystal Growth Design* 10: 2888–2894. https://pubs.acs.org/doi/full/10.1021/cg900920q
17. Amendola V, Riello P, Meneghetti M (2011) Magnetic nanoparticles of iron carbide, iron oxide, iron@iron oxide, and metal iron synthesized by laser ablation in organic solvents. *J Phys Chem C* 115: 5140–5146. https://pubs.acs.org/doi/full/10.1021/jp109371m
18. Novoselova LY (2021) Nanoscale magnetite: New synthesis approach, structure and properties. *Appl Surf Sci* 539: 148275. https://doi.org/10.1016/j.apsusc.2020.148275
19. Kolchanov DS, Slabov V, Keller K, et al. (2019) Sol–gel magnetite inks for inkjet printing. *J Mater Chem C* 7: 6426–6432. https://doi.org/10.1039/C9TC00311H
20. Menard MC, Takeuchi KJ, Marschilok AC, et al. (2013) Electrochemical discharge of nanocrystalline magnetite: Structure analysis using X-ray diffraction and X-ray absorption spectroscopy. *Phys Chem Chem Phys* 15: 18539–18548. https://doi.org/10.1039/C3CP52870G
21. Zhang S, Li W, Tan B, et al. (2015) One-pot synthesis of ultra-small magnetite nanoparticles on the surface of reduced graphene oxide nanosheets as anodes for sodium-ion batteries. *J Mater Chem A* 3: 4793–4798. https://doi.org/10.1039/C4TA06708H
22. Zaidi SDA, Wang C, György B, et al. (2020) Iron and silicon oxide doped/PAN-based carbon nanofibers as free-standing anode material for Li-ion batteries. *J Colloid Interface Sci* 569: 164–176. https://doi.org/10.1016/j.jcis.2020.02.059
23. Li J, Li Y, Chen X, et al. (2019) Selective synthesis of magnetite nanospheres with controllable morphologies on CNTs and application to lithium-ion batteries. *Phys Status Solidi A* 216: 1800924. https://doi.org/10.1002/pssa.201800924

24. Sajid M, Płotka-Wasylka J (2020) Nanoparticles: Synthesis, characteristics, and applications in analytical and other sciences. *Microchem J* 154: 104623. https://doi.org/10.1016/j.microc.2020.104623
25. Mohamed G, Hassan N, Shahat A, et al. (2021) Synthesis and characterization of porous magnetite nanosphere iron oxide as a novel adsorbent of anionic dyes removal from aqueous solution. *Biointerface Res Appl Chem* 11: 13377–13401. https://doi.org/10.33263/BRIAC115.1337713401
26. Masuku M, Ouma L, Pholosi A, et al. (2021) Microwave-assisted synthesis of oleic acid-modified magnetite nanoparticles for benzene adsorption. *Environ Nanotechnol Monit Manag* 15: 100429. https://doi.org/10.1016/j.enmm.2021.100429
27. Jalil MA, Halim AFMF, Moniruzzaman M, et al. (2023) Nano materials in textile processing, In: Rahman MM, Mashud M, Rahman MM, *Advanced Technology in Textiles. Textile Science and Clothing Technology*, Singapore: Springer Nature. https://doi.org/10.1007/978-981-99-2142-3_12
28. Saif S, Tahir A, Chen Y, et al. (2016) Green synthesis of iron nanoparticles and their environmental applications and implications. *Nanomaterials* 6: 209. https://doi.org/10.3390/nano6110209
29. Bruschi ML, de Toledo LDAS (2019) Pharmaceutical applications of iron-oxide magnetic nanoparticles. *Magnetochemistry* 5: 50. https://doi.org/10.3390/magnetochemistry5030050
30. Ghazanfari MR, Kashefi M, Shams SF, et al. (2016) Perspective of Fe_3O_4 nanoparticles' role in biomedical applications. *Biochem Res Int* 2016: 7840161. https://doi.org/10.1155/2016/7840161
31. Gao G, Shi R, Qin W, et al. (2010) Solvothermal synthesis and characterization of size-controlled monodisperse Fe_3O_4 nanoparticles. *J Mater Sci* 45: 3483–3489. https://doi.org/10.1007/s10853-010-4378-7
32. Satvekar RK, Rohiwal SS, Tiwari AP, et al. (2015) Sol–gel derived silica/chitosan/Fe_3O_4 nanocomposite for direct electrochemistry and hydrogen peroxide biosensing. *Mater Res Express* 2: 015402. https://doi.org/10.1088/2053-1591/2/1/015402
33. Manikandan A, Vijaya JJ, Mary JA, et al. (2014) Structural, optical, and magnetic properties of Fe_3O_4 nanoparticles prepared by a facile microwave combustion method. *J Ind Eng Chem* 20: 2077–2085. https://doi.org/10.1016/j.jiec.2013.09.035
34. Kalantari K, Ahmad MB, Shameli K, et al. (2013) Synthesis of talc/Fe_3O_4 magnetic nanocomposites using the chemical co-precipitation method. *Int J Nanomedicine* 8: 1817–1823. https://doi.org/10.2147/IJN.S43693
35. Wu S, Sun A, Zhai F, et al. (2011) Fe_3O_4 magnetic nanoparticles synthesis from tailings by ultrasonic chemical co-precipitation. *Mater Lett* 65: 1882–1884. https://doi.org/10.1016/j.matlet.2011.03.065
36. Osman AI, Zhang Y, Farghali M, et al. (2024) Synthesis of green nanoparticles for energy, biomedical, environmental, agricultural, and food applications: A review. *Environ Chem Lett* 22: 841–887. https://doi.org/10.1007/s10311-023-01682-3
37. Sánchez-López E, Gomes D, Esteruelas G, et al. (2020) Metal-based nanoparticles as antimicrobial agents: An overview. *Nanomaterials* 10: 292. https://doi.org/10.3390/nano10020292
38. Kumar PSR, Alexis SJ (2019) Synthesized carbon nanotubes and their applications, In: Yaragalla S, Mishra R, Thomas S, et al. *Carbon-Based Nanofillers and Their Rubber Nanocomposites*, Amsterdam: Elsevier, 109–122. https://doi.org/10.1016/B978-0-12-813248-7.00004-3

39. Singh P, Kim YJ, Zhang D, et al. (2016) Biological synthesis of nanoparticles from plants and microorganisms. *Trends Biotechnol* 34: 588–599. https://doi.org/10.1016/j.tibtech.2016.02.006
40. Mihai AD, Chircov C, Grumezescu AM, et al. (2020) Magnetite nanoparticles and essential oil systems for advanced antibacterial therapies. *Int J Mol Sci* 21: 7355. https://doi.org/10.3390/ijms21197355
41. Prabhu NN (2018) Green synthesis of iron oxide nanoparticles (IONPs) and their nanotechnological applications. *J Bacteriol Mycol Open Access* 6: 260–262. https://doi.org/10.15406/jbmoa.2018.06.00215
42. López YC, Antuch M (2020) Morphology control in the plant-mediated synthesis of magnetite nanoparticles. *Curr Opin Green Sustainable Chem* 24: 32–37. https://doi.org/10.1016/j.cogsc.2020.02.001
43. Rathinavel S, Priyadharshini K, Panda D (2021) A review on carbon nanotube: An overview of synthesis, properties, functionalization, characterization, and the application. *Mater Sci Eng B* 268: 115095. https://doi.org/10.1016/j.mseb.2021.115095
44. Ma Z, Mohapatra J, Wei K, et al. (2021) Magnetic nanoparticles: Synthesis, anisotropy, and applications. *Chem Rev* 123: 3904–3943. https://doi.org/10.1021/acs.chemrev.1c00860
45. Rattan S, Derek Fawcett D, Poinern GEJ, et al. (2021) Williamson-Hall-based X-ray peak profile evaluation and nano-structural characterization of rod-shaped hydroxyapatite powder for potential dental restorative procedures. *AIMS Mater Sci* 8: 359–372. https://doi.org/10.3934/matersci.2021023
46. Ayeshamariam A, Sanjeeviraja C, Jayachandran M, et al. (2011) Synthesization, characterization, and gas sensing properties of SnO_2 nanoparticles. *Int J Chem Anal Sci* 2: 54–61. https://doi.org/10.1166/jno.2013.1471
47. Cullity BD, Smoluchowski R (1957) Elements of X-ray diffraction. *Phys Today* 10: 50. https://doi.org/10.1063/1.3060306
48. Aly KA, Khalil NM, Algamal Y, et al. (2016) Lattice strain estimation for $CoAl_2O_4$ nanoparticles using Williamson-Hall analysis. *J Alloys Compd* 676: 606–612. https://doi.org/10.1016/j.jallcom.2016.03.213
49. Harjo S, Tomota Y, Torii S, et al. (2002) Residual thermal phase stresses in α–γ Fe–Cr–Ni alloys measured by a neutron diffraction time-of-flight method. *Mater Trans* 43: 1696–1702. https://doi.org/10.2320/matertrans.43.1696
50. Biju V, Sugathan N, Vrinda V, et al. (2008) Estimation of lattice strain in nanocrystalline silver from X-ray diffraction line broadening. *J Mater Sci* 43: 1175–1179. https://doi.org/10.1007/s10853-007-2300-8
51. Ravinder D, Alivelumanga T (1998) Composition dependence of elastic behaviour of mixed manganese–zinc ferrites. *Mater Lett* 37: 51–56. https://doi.org/10.1016/S0167-577X(98)00062-7
52. Yusefi M, Shameli K, Ali RR, et al. (2020) Evaluating anticancer activity of plant-mediated synthesized iron oxide nanoparticles using *Punica granatum* fruit peel extract. *J Mol Struct* 1204: 127539. https://doi.org/10.1016/j.molstruc.2019.127539
53. Izadiyan Z, Shameli K, Miyake M, et al. (2020) Cytotoxicity assay of plant-mediated synthesized iron oxide nanoparticles using *Juglans regia* green husk extract. *Arab J Chem* 13: 2011–2023. https://doi.org/10.1016/j.arabjc.2018.02.019
54. Hearmon RFS (1956) The elastic constants of anisotropic materials—II. *Adv Phys* 5: 323–382. https://doi.org/10.1080/00018732.1956.tADP0323

55. Chaki SH, Malek TJ, Chaudhary MD, et al. (2015) Magnetite Fe_3O_4 nanoparticles synthesis by wet chemical reduction and their characterization. *Adv Nat Sci Nanosci Nanotechnol* 6: 035009. https://doi.org/10.1088/2043-6262/6/3/035009
56. Yusoff AHM, Salimi MN, Jamlos MF (2017) Dependence of lattice strain of magnetite nanoparticles on precipitation temperature and pH of solution. *J Phys Conf Ser* 908: 012065. https://doi.org/10.1088/1742-6596/908/1/012065
57. Kushwaha P, Chauhan P (2021) Microstructural evaluation of iron oxide nanoparticles at different calcination temperature by Scherrer, Williamson-Hall, Size-Strain Plot and Halder-Wagner methods. *Phase Transit* 94: 731–753. https://doi.org/10.1080/01411594.2021.1969396
58. Ilyas S, Abdullah B, Tahir D (2019) X-ray diffraction analysis of nanocomposite Fe_3O_4/activated carbon by Williamson-Hall and size-strain plot methods. *Nano Struct Nano Objects* 20: 100396. https://doi.org/10.1016/j.nanoso.2019.100396
59. Yusefi M, Shameli K, Ali RR, et al. (2020) Evaluating anticancer activity of plant-mediated synthesized iron oxide nanoparticles using *Punica granatum* fruit peel extract. *J Mol Struct* 1204: 127539. https://doi.org/10.1016/j.molstruc.2019.127539
60. Vives S, Gaffet E, Meunier C (2004) X-ray diffraction line profile analysis of iron ball milled powders. *Mater Sci Eng A* 366: 229–238. https://doi.org/10.1016/S0921-5093(03)00572-0
61. Jafari A, Farjami Shayesteh S, Salouti M, et al. (2015) Dependence of structural phase transition and lattice strain of Fe_3O_4 nanoparticles on calcination temperature. *Indian J Phys* 89: 551–560. https://doi.org/10.1007/s12648-014-0627-y
62. Zak AK, Majid WA, Abrishami ME, et al. (2011) X-ray analysis of ZnO nanoparticles by Williamson-Hall and size–strain plot methods. *Solid State Sci* 13: 251–256. https://doi.org/10.1016/j.solidstatesciences.2010.11.024
63. Rana G, Johri UC (2014) Correlation between the pH value and properties of magnetite nanoparticles. *Adv Mater Lett* 5: 280–286. https://doi.org/10.5185/amlett.2014.10563
64. Gholizadeh A (2017) A comparative study of physical properties in Fe_3O_4 nanoparticles prepared by coprecipitation and citrate methods. *J Am Ceram Soc* 100: 3577–3588. https://doi.org/10.1111/jace.14896
65. Suppiah DD, Abd Hamid SB (2016) One step facile synthesis of ferromagnetic magnetite nanoparticles. *J Magn Magn Mater* 414: 204–208. https://doi.org/10.1016/j.jmmm.2016.04.072
66. Da'na E, Taha A, Afkar E (2018) Green synthesis of iron nanoparticles by *Acacia nilotica* pods extract and its catalytic, adsorption, and antibacterial activities. *Appl Sci* 8: 1922. https://doi.org/10.3390/app8101922
67. Van Ommen JR, Valverde JM, Pfeffer R (2012) Fluidization of nanopowders: A review. *J Nanopart Res* 14: 1–29. https://doi.org/10.1007/s11051-012-0737-4
68. Bassim S, Mageed AK, AbdulRazak AA, et al. (2022) Green synthesis of Fe_3O_4 nanoparticles and its applications in wastewater treatment. *Inorganics* 10: 260. https://doi.org/10.3390/inorganics10120260
69. Wei R, Li H, Lin Y, et al. (2020) Reduction characteristics of iron oxide by the hemicellulose, cellulose, and lignin components of biomass. *Energy Fuels* 34: 8332–8339. https://doi.org/10.1021/acs.energyfuels.0c00377
70. Laid TM, Abdelhamid K, Eddine LS, et al. (2021) Optimizing the biosynthesis parameters of iron oxide nanoparticles using central composite design. *J Mol Struct* 1229: 129497. https://doi.org/10.1016/j.molstruc.2020.129497

71. Anukam AI, Berghel J, Famewo EB, et al. (2020) Improving the understanding of the bonding mechanism of primary components of biomass pellets through the use of advanced analytical instruments. *J Wood Chem Technol* 40: 15–32. https://doi.org/10.1080/02773813.2019.1652324
72. Ramesh AV, Rama Devi D, Mohan Botsa S, et al. (2018) Facile green synthesis of Fe_3O_4 nanoparticles using aqueous leaf extract of *Zanthoxylum armatum* DC. for efficient adsorption of methylene blue. *J Asian Ceram Soc* 6: 145–155. https://doi.org/10.1080/21870764.2018.1459335
73. Netala VR, Kotakadi VS, Nagam V, et al. (2015) First report of biomimetic synthesis of silver nanoparticles using aqueous callus extract of *Centella asiatica* and their antimicrobial activity. *Appl Nanosci* 5: 801–807. https://doi.org/10.1007/s13204-014-0374-6
74. Awwad AM, Salem NM (2012) A green and facile approach for synthesis of magnetite nanoparticles. *Nanoscience Nanotechnol* 2: 208–213. https://doi.org/10.5923/j.nn.20120206.09
75. Arokiyaraj S, Saravanan M, Prakash NU, et al. (2013) Enhanced antibacterial activity of iron oxide magnetic nanoparticles treated with *Argemone mexicana* L. leaf extract: An in vitro study. *Mater Res Bull* 48: 3323–3327. https://doi.org/10.1016/j.materresbull.2013.05.059
76. Rahmani R, Gharanfoli M, Gholamin M, et al. (2020) Plant-mediated synthesis of superparamagnetic iron oxide nanoparticles (SPIONs) using aloe vera and flaxseed extracts and evaluation of their cellular toxicities. *Ceram Int* 46: 3051–3058. https://doi.org/10.1016/j.ceramint.2019.10.005
77. Rahmayanti M, Syakina AN, Fatimah I, et al. (2022) Green synthesis of magnetite nanoparticles using peel extract of jengkol (*Archidendron pauciflorum*) for methylene blue adsorption from aqueous media. *Chem Phys Lett* 803: 139834. https://doi.org/10.1016/j.cplett.2022.139834
78. Ghoohestani E, Samari F, Homaei A, et al. (2024) A facile strategy for preparation of Fe_3O_4 magnetic nanoparticles using *Cordia myxa* leaf extract and investigating its adsorption activity in dye removal. *Sci Rep* 14: 84. https://doi.org/10.1038/s41598-023-50550-1
79. Hasan K, Shehadi IA, Al-Bab ND, et al. (2019) Magnetic chitosan-supported silver nanoparticles: A heterogeneous catalyst for the reduction of 4-nitrophenol. *Catalysts* 9: 839. https://doi.org/10.3390/catal9100839
80. Halim AF, Poinern GE, Fawcett D, et al. (2024) Green biogenic synthesis of magnetite nanoparticles from indigenous *Banksia ashbyi* leaf for enhanced sonochemical dye degradation. *Mater Res Express*. https://doi.org/10.1088/2053-1591/ad8ca0
81. Yusefi M, Shameli K, Yee OS, et al. (2021) Green synthesis of Fe_3O_4 nanoparticles stabilized by a *Garcinia mangostana* fruit peel extract for hyperthermia and anticancer activities. *Int J Nanomed* 16: 2515. https://doi.org/10.2147/IJN.S284134
82. Yuvakkumar R, Hong SI (2014) Green synthesis of spinel magnetite iron oxide nanoparticles. *Adv Mater Res* 1051: 39–42. https://doi.org/10.4028/www.scientific.net/AMR.1051.39
83. Murugappan K, Silvester DS, Chaudhary D, et al. (2014) Electrochemical characterization of an oleyl-coated magnetite nanoparticle-modified electrode. *ChemElectroChem* 1: 1211–1218. https://doi.org/10.1002/celc.201402012
84. Mishra AK, Ramaprabhu S (2011) Nano magnetite decorated multiwalled carbon nanotubes: A robust nanomaterial for enhanced carbon dioxide adsorption. *Energy Environ Sci* 4: 889–895. https://doi.org/10.1039/C0EE00076K
85. Konon M, Brazovskaya EY, Kreisberg V, et al. (2023) Novel inorganic membranes based on magnetite-containing silica porous glasses for ultrafiltration: Structure and sorption properties. *Membranes* 13: 341. https://doi.org/10.3390/membranes13030341

86. Taha AB, Essa MS, Chiad BT (2023) Iron oxide nanoparticles preparation by using homemade hydrothermal pyrolysis technique with different reaction times. *J Metastable Nanocryst Mater* 35: 1–10. https://doi.org/10.4028/p-cbng1t
87. Sheng-Nana S, Chaoa W, Zan-Zanb Z, et al. (2014) Magnetic iron oxide nanoparticles: Synthesis and surface coating techniques for biomedical applications. *Chin Phys B* 23: 037503–037519. https://doi.org/10.1088/1674-1056/23/3/037503
88. Yew YP, Shameli K, Miyake M, et al. (2016) Green synthesis of magnetite (Fe_3O_4) nanoparticles using seaweed (*Kappaphycus alvarezii*) extract. *Nanoscale Res Lett* 11: 1–7. https://doi.org/10.1186/s11671-016-1498-2
89. Das C, Sen S, Singh T, et al. (2020) Green synthesis, characterization, and application of natural product coated magnetite nanoparticles for wastewater treatment. *Nanomaterials* 10: 1615. https://doi.org/10.3390/nano10081615
90. Basavegowda N, Magar KBS, Mishra K, et al. (2014) Green fabrication of ferromagnetic Fe_3O_4 nanoparticles and their novel catalytic applications for the synthesis of biologically interesting benzoxazinone and benzthioxazinone derivatives. *New J Chem* 38: 5415–5420. https://doi.org/10.1039/C4NJ01155D
91. Basavegowda N, Mishra K, Lee YR (2014) Sonochemically synthesized ferromagnetic Fe_3O_4 nanoparticles as a recyclable catalyst for the preparation of pyrrolo[3,4-c]quinoline-1,3-dione derivatives. *RSC Adv* 4: 61660–61666. https://doi.org/10.1039/C4RA11623B
92. Afzal S, Khan R, Zeb T, et al. (2018) Structural, optical, dielectric, and magnetic properties of PVP coated magnetite (Fe_3O_4) nanoparticles. *J Mater Sci Mater Electron* 29: 20040–20050. https://doi.org/10.1007/s10854-018-0134-6
93. Khan R, Rahman MU, Iqbal Z (2016) Variation of structural, dielectric, and magnetic properties of PVP coated γ-Fe_2O_3 nanoparticles. *J Mater Sci Mater Electron* 27: 12490–12498. https://doi.org/10.1007/s10854-016-5634-7
94. Mirza I, Sarfraz A, Hasanain S (2014) Effect of surfactant on magnetic and optical properties of α-Fe_2O_3 nanoparticles. *Acta Phys Pol A* 126: 1280–1287. https://doi.org/10.12693/APhysPolA.126.1280
95. Attallah OA, Al-Ghobashy MA, Nebsen M, et al. (2018) Assessment of pectin-coated magnetite nanoparticles in low-energy water desalination applications. *Environ Sci Pollut Res* 25: 18476–18483. https://doi.org/10.1007/s11356-018-2060-9
96. Basavaiah K, Kahsay MH, Rama Devi D (2018) Green synthesis of magnetite nanoparticles using aqueous pod extract of *Dolichos lablab* L for efficient adsorption of crystal violet. *Emergent Mater* 1: 121–132. https://doi.org/10.1007/s42247-018-0005-1
97. Awwad AM, Salem NM (2012) A green and facile approach for synthesis of magnetite nanoparticles. *Nanosc Nanotechnol* 2: 208–213. https://doi.org/10.5923/j.nn.20120206.09
98. ISO 14040:2006. Environmental management-Life cycle assessment-Principles and framework. Available from: https://www.iso.org/standard/37456.html (accessed August 25, 2021).
99. ISO 14044:2006. Environmental management-Life cycle assessment-Requirements and guidelines. Available from: https://www.iso.org/standard/38498.html (accessed August 25, 2021).

100. Al-Hazeef MS, Aidi A, Hecini L, et al. (2024) Valorizing date palm spikelets into activated carbon-derived composite for methyl orange adsorption: Advancing circular bio-economy in wastewater treatment—A comprehensive study on its equilibrium, kinetics, thermodynamics, and mechanisms. *Environ Sci Pollut Res* 1–20. https://doi.org/10.1007/s11356-024-34581-3

AIMS Press